

Transport properties of Hall-type quantum states in disordered bismuthene

Jiaojiao Zhou(周娇娇), Jiangying Yu(余江应), Shuguang Cheng(成淑光), and Hua Jiang(江华)

Citation: Chin. Phys. B, 2024, 33 (**4**): 047105. DOI: 10.1088/1674-1056/ad2605
Journal homepage: http://cpb.iphy.ac.cn; http://iopscience.iop.org/cpb

What follows is a list of articles you may be interested in

Intrinsic V vacancy and large magnetoresistance in $V_{1-\delta}Sb_2$ single crystal

Yong Zhang(张勇), Xinliang Huang(黄新亮), Jinglei Zhang(张警蕾), Wenshuai Gao(高文帅), Xiangde Zhu(朱相德), and Li Pi(皮雳)

Chin. Phys. B, 2022, 31 (**3**): 037102. DOI: 10.1088/1674-1056/ac3070

Tuning transport coefficients of monolayer $MoSi_2N_4$ with biaxial strain

Xiao-Shu Guo(郭小姝) and San-Dong Guo(郭三栋)

Chin. Phys. B, 2021, 30 (**6**): 067102. DOI: 10.1088/1674-1056/abdb22

Vanadium based XVO_3 (X=Na, K, Rb) as promising thermoelectric materials: First-principle DFT calculations

N A Noor, Nosheen Mushahid, Aslam Khan, Nessrin A. Kattan, Asif Mahmood, Shahid M. Ramay

Chin. Phys. B, 2020, 29 (**9**): 097101. DOI: 10.1088/1674-1056/ab99ad

Effects of layer stacking and strain on electronic transport in two-dimensional tin monoxide

Yanfeng Ge(盖彦峰), Yong Liu(刘永)

Chin. Phys. B, 2019, 28 (**7**): 077104. DOI: 10.1088/1674-1056/28/7/077104

Negative differential resistance and quantum oscillations in $FeSb_2$ with embedded antimony

Fangdong Tang(汤方栋), Qianheng Du(杜乾衡), Cedomir Petrovic, Wei Zhang(张威), Mingquan He(何明全), Liyuan Zhang(张立源)

Chin. Phys. B, 2019, 28 (**3**): 037104. DOI: 10.1088/1674-1056/28/3/037104

SPECIAL TOPIC — Valleytronics

Transport properties of Hall-type quantum states in disordered bismuthene

Jiaojiao Zhou(周娇娇)[1], Jiangying Yu(余江应)[1], Shuguang Cheng(成淑光)[2,†], and Hua Jiang(江华)[3,‡]

[1] *Key Laboratory of Advanced Electronic Materials and Devices, School of Mathematics and Physics, Anhui Jianzhu University, Hefei* 230601, *China*
[2] *Department of Physics, Northwest University, Xi'an* 710069, *China*
[3] *School of Physical Science and Technology, Soochow University, Suzhou* 215006, *China*

(Received 9 December 2023; revised manuscript received 19 January 2024; accepted manuscript online 5 February 2024)

Bismuthene, an inherently hexagonal structure characterized by a huge bulk gap, offers a versatile platform for investigating the electronic transport of various topological quantum states. Using nonequilibrium Green's function method and Landauer–Büttiker formula, we thoroughly investigate the transport properties of various Hall-type quantum states, including quantum spin Hall (QSH) edge states, quantum valley Hall kink (QVHK) states, and quantum spin–valley Hall kink (QSVHK) states, in the presence of various disorders. Based on the exotic transport features, a spin–valley filter, capable of generating a highly spin- and valley-polarized current, is proposed. The valley index and the spin index of the filtered QSVHK state are determined by the staggered potential and the intrinsic spin–orbit coupling, respectively. The efficiency of the spin–valley filter is supported by the spacial current distribution, the valley-resolved conductance, and the spin-resolved conductance. Compared with a sandwich structure for QSVHK, our proposed spin–valley filter can work with a much smaller size and is more accessible in the experiment.

Keywords: electronic transport, bismuthene, spin–valley filter

PACS: 71.15.–m, 73.20.–r, 73.23.–b, 73.63.–b **DOI:** 10.1088/1674-1056/ad2605

1. Introduction

The transport of topological states is a prominent area of interest in low-dimensional condensed matter physics.[1–7] In such states, gapless edge modes exist within the bulk band gap, exhibiting exotic transport behaviors which robust against disorder.[8,9] In particular, in quantum spin Hall (QSH) edge states, carriers with different spins flow in opposite directions along the boundaries.[10–12] The quantum valley Hall kink (QVHK) states are located at the interface of two hexagonal lattice materials with different valley-projected topological charges.[13–16] Carriers from one valley will flow in a direction, while those from the other valley will flow in the opposite direction at the interface. When the spin- and valley-projected topological charges are different on both sides of the interface, the QSH edge states and QVHK states emerge simultaneously, leading to the formation of a novel quantum state, referred to as quantum spin–valley Hall kink (QSVHK) state.[17–19] In this state, the spin-up state propagating forward along the interface belongs to the K valley, and the spin-down state propagating backward belongs to the K' valley.

Two-dimensional hexagonal structures, such as graphene, have a variety of controllable features,[20–22] including charge, spin, and valley degrees of freedom. Nevertheless, owing to the weak spin–orbit coupling of graphene, the tiny bulk gap is only about 40 μeV, limiting its application for quantum devices.[23] Subsequently, the graphene-like structures with a strong spin–orbit coupling, such as arsenene,[24,25] antimonene,[26–29] bisthumene,[30–35] transition metal dichalcogenides,[36–38] are investigated. Remarkably, the bismuthene on SiC substrate has a huge topological bulk gap,[30] rendering the application of quantum devices feasible. Intriguingly, it is possible to modulate the parameters in the bismuthene structure, such as the spin–orbit coupling strength λ_{SOC} or the staggered potential U. The adjustment of λ_{SOC} can be achieved through substrate selection and chemical surface functionalization,[25,39] while U can be controlled via alloy engineering or the application of a vertical electric field.[39,40] When $\lambda_{\mathrm{SOC}} > U$, the structure exhibits as a QSH system.[4,5] Conversely, when $\lambda_{\mathrm{SOC}} < U$, the structure behaves as a QVH system.[36,41]

In this paper, we thoroughly investigate the transport properties of the various Hall-type quantum states in the zigzag bismuthene ribbons, as illustrated in Fig. 1(a). By tuning the staggered potential and the intrinsic spin–orbit coupling strength, the QSH edge, QVHK, and QSVHK states can be studied. We analyze the impact of combined Anderson/long-range and magnetic/non-magnetic disorders on these states. Specifically, the transport of QSH edge state is susceptible to magnetic disorder and the transport of the QVHK state is obstructed by Anderson disorder. However,

[†]Corresponding author. E-mail: sgcheng@nwu.edu.cn
[‡]Corresponding author. E-mail: jianghuaphy@suda.edu.cn

© 2024 Chinese Physical Society and IOP Publishing Ltd

QSVHK states combine the advantages of both, they are robust against non-magnetic Anderson disorder, long-range non-magnetic disorder, and long-range magnetic disorder. Guaranteed by the fragility of the QSH edge states and the robustness of the QSVHK states under long-range magnetic disorder, we propose a spin–valley filter based on a QSH–QVH heterostructure. The numerical calculation demonstrates that the expected current component with specific valley and spin indices is robust against disorder and other components are depleted. The output of the spin–valley filter is controllable since the valley index is determined by the staggered potential which can be altered by an external electric field. Compared with the sandwich structure hosting QSVHK states, our proposed spin–valley filter is able to work in a narrow device and the output has only one component.

This paper is organized as follows. In Section 2, we introduce the tight-binding models and the numerical method for calculating the conductance, including Green's function method and the transfer matrix method. In Section 3, we first explore the key transport characteristics of three types of topological states and their features under various disorders and interface profiles. By using the exotic transport behaviors of the topological states, a spin–valley filter is proposed and the transport properties are thoroughly studied. Finally, a concise conclusion is provided in Section 4.

2. Theoretical method

Here, we utilize bismuthene nanoribbons, as illustrated in Fig. 1(a), as a platform. The gray area separates the ribbon into three parts: left terminal, central region, and right terminal, respectively. Disorder effects are specifically considered only in the central region. The tight-binding representation of the Hamiltonian for the bismuthene models[42] is expressed as the summation of two parts, written as

$$\begin{aligned} H &= H_0 + H_{\rm D}, \\ H_0 &= \sum_{j=1}^{3} c_{\boldsymbol{i}}^{+} T_{\boldsymbol{\delta}_j} c_{\boldsymbol{i}+\boldsymbol{\delta}_j} + \text{h.c.} \\ &\quad + \sum_{\boldsymbol{i}} c_{\boldsymbol{i}}^{+} [\lambda_{\rm SOC} \boldsymbol{\tau}_z \otimes \boldsymbol{\sigma}_z] c_{\boldsymbol{i}} + \sum_{\boldsymbol{i}} c_{\boldsymbol{i}}^{+} [U_i \boldsymbol{\tau}_0 \otimes \boldsymbol{\sigma}_0] c_{\boldsymbol{i}}, \\ H_{\rm D} &= \sum_{\boldsymbol{i}} c_{\boldsymbol{i}}^{+} \eta_i \begin{pmatrix} 1 & 1 \\ 1 & 1 \end{pmatrix} \otimes \boldsymbol{\sigma}_{0/x} c_{\boldsymbol{i}}. \end{aligned} \tag{1}$$

The first part H_0 describes the clean model without disorder. Here, $c_{\boldsymbol{i}}$ and $c_{\boldsymbol{i}}^{+}$ are the annihilation and creation operators of electrons at site $\boldsymbol{i}$. $\boldsymbol{\sigma}_z$ and $\boldsymbol{\tau}_z$ are the Pauli matrices acting in spin and orbital space, respectively. $\boldsymbol{\sigma}_0$ and $\boldsymbol{\tau}_0$ are the identity matrix. The term

$$T_{\boldsymbol{\delta}_j} = \begin{pmatrix} t & z^{(3-j)}t \\ z^{j}t & t \end{pmatrix} \otimes \boldsymbol{\sigma}_0$$

describes the nearest hopping from site $\boldsymbol{i}$ to the nearest site $\boldsymbol{i}+\boldsymbol{\delta}_j$, as illustrated in Fig. 1(a), with $z = \mathrm{e}^{\mathrm{i}2\pi/3}$ as a constant and t as the hopping coefficient. $\lambda_{\rm SOC}$ represents the intrinsic spin–orbit coupling strength. The staggered potential in the A (B) sublattice $U_i = U$ $(-U)$ can be achieved through chemical surface functionalization.[43] The second part $H_{\rm D}$ accounts for the disorder, where the on-site energy at site $\boldsymbol{i}$ is $\eta_i = \sum_{j=1}^{N_k} \omega_j \mathrm{e}^{-r_{ij}^2/\xi^2}$. Here, r_{ij} denotes the distance between the site $\boldsymbol{i}$ and $\boldsymbol{j}$, ξ represents the spatial correlation parameter, N_k is the total number of the scattering scatters, and ω_j is the disorder randomly distributed in $[-W, W]$ with W being the disorder strength. In the scenario of Anderson disorder with $N_k = \mathcal{N}$, $\mathcal{N}$ is the number of atoms in the central region, and $\eta_i = \omega_j$ under $\xi \to 0$. While in the long-range disorder with $N_k = \mathcal{N}/100$, we set $\xi = 5a$, where a is the lattice constant. In non-magnetic disorder, an identity matrix $\boldsymbol{\sigma}_0$ acts on spin space. In magnetic disorder, the Pauli matrix $\boldsymbol{\sigma}_x$ acts on spin space. The transmission coefficients are averaged up to 500 configurations for each value of disorder strength.

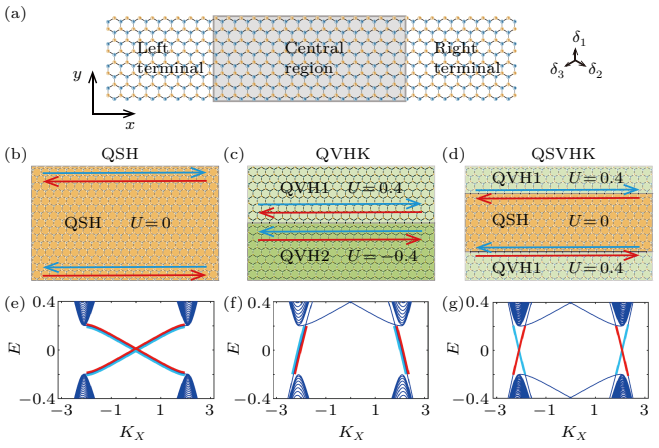


Fig. 1. (a) The schematic of the bismuthene nanoribbon. The grey region, with $N = 4$ and $L = 15$, divides the ribbon into left terminal, central region, and right terminal. (b)–(d) The structures and (e)–(g) their energy bands of QSH, QVH–QVH, and QVH–QSH–QVH nanoribbons. The red and blue arrows represent the spin-up and the spin-down states, respectively. In the QSH ribbon, QSH edge states are localized at the boundaries. In the QVH–QVH ribbon, two pairs of spin degenerate QVHK states emerge along the interface between the QVH1 and QVH2 regions. In the QVH–QSH–QVH ribbon, the spin–valley locked QSVHK states are distributed at two interfaces between the QVH1 and QSH regions. The spin–orbit coupling strength is $\lambda_{\rm SOC} = 0.2$ eV. The staggered potentials of these regions are $U(\text{QVH1}) = 0.4$ eV, $U(\text{QVH2}) = -0.4$ eV and $U(\text{QSH}) = 0$ eV. The energy bands are calculated with $N(\text{QSH}) = 80$ in QSH nanoribbons, $N(\text{QVH1}) = 40$ and $N(\text{QVH2}) = 40$ in QVH–QVH nanoribbons, $N(\text{QVH1}) = 20$ and $N(\text{QSH}) = 40$ in QVH–QSH–QVH nanoribbons.

To characterize the transport properties of the quantum states, the zero-temperature electrical differential conductance $G(E)$ at the Fermi energy E is presented. Utilizing the nonequilibrium Green's function method and Landauer-Büttiker formula, $G(E)$ under a small bias can be expressed as

$$G(E) = \frac{e^2}{h} \mathrm{Tr}[\boldsymbol{\Gamma}_{\rm L}(E) \boldsymbol{G}^{\rm r}(E) \boldsymbol{\Gamma}_{\rm R}(E) \boldsymbol{G}^{\rm a}(E)], \tag{2}$$

where $\boldsymbol{\Gamma}_p(E) = \mathrm{i}[\boldsymbol{\Sigma}_p^{\mathrm{r}}(E) - \boldsymbol{\Sigma}_p^{\mathrm{a}}(E)]$ represents the linewidth function of the terminals ($p = \mathrm{L}, \mathrm{R}$) and $\boldsymbol{G}^{\mathrm{r}}(E) = [\boldsymbol{G}^{\mathrm{a}}(E)]^{\dagger} = 1/[(E - \boldsymbol{H}_{\mathrm{C}}) - \boldsymbol{\Sigma}_{\mathrm{L}}^{\mathrm{r}} - \boldsymbol{\Sigma}_{\mathrm{R}}^{\mathrm{r}}]$ denotes the retarded Green's function.[44] The self-energy $\boldsymbol{\Sigma}_p^{\mathrm{r}}$ of the semi-infinite terminal-p can be calculated via a transfer matrix method,[45–48] and $\boldsymbol{H}_{\mathrm{C}}$ represents the Hamiltonian in the central region. In the left and right terminals, the energy is shifted by gate voltages to ensure enough conductive channels from the bulk states. By applying a small voltage bias $V = V_{\mathrm{L}} - V_{\mathrm{R}}$ between the left and right terminals, the local current between the sites $\boldsymbol{i}$ and $\boldsymbol{j}$ can be expressed as[49–51]

$$J_{i\to j}(E) = \frac{2e^2V}{h}\mathrm{Im}\{H_{ij}[\boldsymbol{G}^{\mathrm{r}}(E)\boldsymbol{\Gamma}_{\mathrm{L}}(E)\boldsymbol{G}^{\mathrm{a}}(E)]\}_{ij}. \tag{3}$$

Since the spin ($\alpha = \uparrow, \downarrow$) is a good quantum number in both terminals, one can obtain the spin differential conductances $G_{\uparrow}$ and $G_{\downarrow}$ by

$$G_{\alpha}(E) = \frac{e^2}{h}\mathrm{Tr}[\boldsymbol{\Gamma}_{\alpha\mathrm{L}}(E)\boldsymbol{G}^{\mathrm{r}}(E)\boldsymbol{\Gamma}_{\alpha\mathrm{R}}(E)\boldsymbol{G}^{\mathrm{a}}(E)], \tag{4}$$

with e being the electron charge and h being the Planck's constant. And the valley-resolved conductances $G_{K/K'}$ are obtained via the transfer matrix method.[52,53] With such a method, each component τ_{k_1,k_2}, representing the transmission amplitude from state k_1 in the left terminal to state k_2 in the right terminal, is calculated. Then, the valley-resolved conductance is calculated as follows:

$$G_{K/K'}(E) = \frac{e^2}{h}\sum_{k_1}\sum_{k_2\in K/K'}\tau_{k_1,k_2}(E). \tag{5}$$

The first summation counts for all the right-going transmission states in the left terminal, while the second summation only records the states from the central region and ends up with the valley K/K' in the right terminal.

3. Results and discussion

In the model illustrated in Fig. 1(a), when $\lambda_{\mathrm{SOC}} > U$, a QSH region with edge states is presented, as depicted in Fig. 1(b). And if $\lambda_{\mathrm{SOC}} < |U|$, it is an insulating QVH region. When two different QVH regions of different topological charges are attached, as shown in Fig. 1(c), QVHK states with spin degeneracy appear on the interface. In the configuration where a QSH region is sandwiched by two QVH regions, as illustrated in Fig. 1(d), the spin–valley locked Hall states, i.e., QSVHK states, are localized at two interfaces. Here, we set the parameter $\lambda_{\mathrm{SOC}} = 0.2$ eV, which is comparable to the fitting parameters of bismuthene from the first-principles data.[54] The magnitude of staggered potential U is set as 0.4 eV/ − 0.4 eV in QVH regions and 0 eV in QSH regions, as illustrated in Figs. 1(b)–1(d). Then, the Hall-type quantum states exist inside the bulk band gap $E \in [-|\lambda_{\mathrm{SOC}} - U|, |\lambda_{\mathrm{SOC}} - U|]$, i.e., $E \in [-0.2, 0.2]$ in Figs. 1(e)–1(g), and the conductance forms a quantized plateau in this range (indicated by the gray dotted line in Figs. 3(a) and 3(b)). To further investigate the role of interface profile in the transport of topological kink states, we first discuss two cases of potential energy variation, the step form and the cosine form. In the subsequent calculation, the lattice constant $a = 5.53$ Å is set as a unit of length, which is also adopted from the first-principles calculations.[42] The hopping $t = 1$ eV is set as an energy unit.

3.1. The step interface

In this subsection, we consider the potential changes from U_1 to U_2 in a step form, i.e., $U(y) = (U_2 - U_1)\Theta(y - y_0) + U_1$, where Θ is the step function, and y_0 represents the location of the interface. Without disorder, the conductances of the QVHK and QSVHK states exhibit a perfect plateau of $2e^2/h$ as the Fermi energy E changes (see the gray dotted line in Fig. 3). The conductances G versus non-magnetic Anderson disorder strength W_{NAD}, long-range non-magnetic disorder strength W_{LND}, magnetic Anderson disorder strength W_{MAD} and long-range magnetic disorder strength W_{LMD} for QSH, QVHK, and QSVHK states are illustrated in Fig. 2.

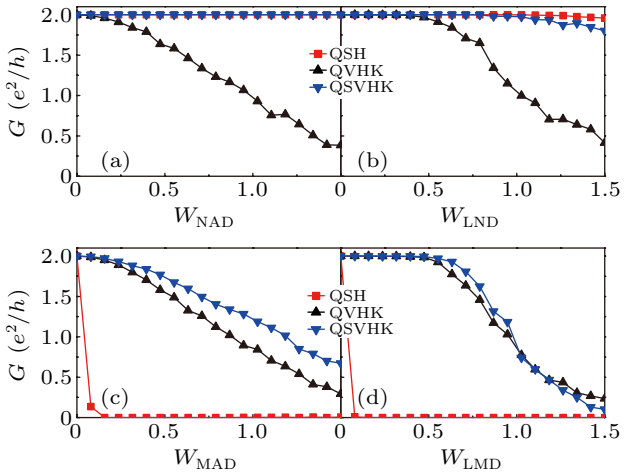


Fig. 2. The conductance of QSH edge, QVHK and QSVHK states versus (a) non-magnetic Anderson disorder strength W_{NAD}, (b) long-range non-magnetic disorder strength W_{LND}, (c) magnetic Anderson disorder strength W_{MAD} and (d) long-range magnetic disorder strength W_{LMD} at $E = 0$. The widths of the ribbons are $N(\mathrm{QSH}) = 80$ in QSH nanoribbons, $N(\mathrm{QVH1}) = 40$ and $N(\mathrm{QVH2}) = 40$ in QVH–QVH nanoribbons, $N(\mathrm{QVH1}) = 20$ and $N(\mathrm{QSH}) = 40$ in QVH–QSH–QVH nanoribbons.

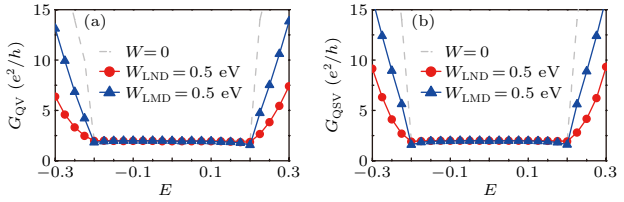


Fig. 3. The conductance G_{QV} and G_{QSV} versus Fermi energy E for QVHK and QSVHK states with $W = 0$, $W_{\mathrm{LND}} = 0.5$ eV and $W_{\mathrm{LMD}} = 0.5$ eV. Other parameters are the same as in Fig. 2.

Under non-magnetic disorders, the conductance of the QSH edge state exhibits a high degree of robustness. Even

if $W_{\rm NAD} = 1.5$ eV or $W_{\rm LND} = 1.5$ eV, the conductance of QSH edge states is hardly affected, due to minimal backscattering occurring only between the same spin states at the two edges, especially when the width of the sample is sufficiently large. However, in the presence of magnetic disorder, the rapid decay of the conductance means the QSH edge states are destroyed easily. As $W_{\rm MAD}$ and $W_{\rm LMD}$ change from 0 to 0.2 eV, the rapid decay of the conductances from $2e^2/h$ to 0 indicates broken time-reversal symmetry caused by magnetic disorder, in agreement with the experimental observations in Fig. 5 of Ref. [55] and Fig. 4(d) of Ref. [56]. Given that magnetic disorder can induce flipping between these spin-up and spin-down states, backscattering becomes easier between these states on the same boundary, resulting in the extreme fragility, that hinders the transmission of the QSH edge state. This characteristic enables us to realize the spin–valley filter under the magnetic disorder, and we will detail it in Subsection 3.3.

The conductances of QVHK states gradually decrease with the increasing Anderson disorder strength, primarily due to the enhanced scattering processes, consistent with the observations illustrated in Fig. 4(b) of Ref. [57]. Since all the forward and backward states concentrate around the interface, backscattering becomes more likely with the increased disorder strength. Nevertheless, under the long-range disorder, the system can still maintain its quantized values within the interval $W_{\rm LND/LMD} \in [0, 0.5]$ protected by space-inversion symmetries. It is noteworthy that QVHK states, being spin degenerate, exhibit immunity to spin-flip induced by magnetic scattering. Consequently, their conductance behaves almost identically in both magnetic and non-magnetic disorder scenarios.

In the presence of non-magnetic disorder, the conductances of QSVHK states experience minimal alteration, as depicted by the blue lines shown in Figs. 2(a) and 2(b). And under the long-range magnetic disorder, with $W_{\rm LMD}$ reaching 0.7 eV, the conductance platform remains stable, indicating a robust transport behavior in the presence of such disorder, as depicted by the blue lines in Fig. 2(d). Unlike the QSH edge states, the QSVHK states have a consistent transmission of spin-polarized current even in the presence of magnetic disorder. Furthermore, in contrast to QVHK state, QSVHK states exhibit a more robust transport of valley-polarized current in the presence of non-magnetic disorder. When compared with the performance of both QVHK and QSH edge states, the QSVHK states are more stable in both magnetic and non-magnetic disorders.

As the conductance platforms tend to emerge under long-range disorder, we investigate the conductances of QVHK and QSVHK states, labeled by $G_{\rm QV}$ and $G_{\rm QSV}$, respectively, versus Fermi energy E under the long-range disorder in Fig. 3. The conductance without the disorder is also plotted in the gray line. Outside the band gap, (i.e., $|E| > 0.2$ eV), we observe $G(W = 0) > G_{\rm QV/QSV}(W_{\rm LMD} = 0.5\ {\rm eV}) > G_{\rm QV/QSV}(W_{\rm LND} = 0.5\ {\rm eV})$, indicating a decrease in the conductances of bulk states with increasing disorder strength. At the same long-range disorder strength and Fermi energy, the influence of magnetic disorder is weaker than that of non-magnetic disorder. Inside the bulk band gap, (i.e., $|E| < 0.2$ eV), it is evident that the conductances $G_{\rm QV}$ and $G_{\rm QSV}$ remain quantized across different Fermi energy E, as illustrated by curves for $W_{\rm LND} = 0.5$ eV and $W_{\rm LMD} = 0.5$ eV in Fig. 3. This result demonstrates that the conductance calculated at $E = 0$ in Fig. 2(d) is reliable.

3.2. The smooth interface

In practice, it is challenging to achieve an atomically sharp potential in experiment.[40] Therefore, it is natural to extend the investigations of the systems to smooth interfaces. In this subsection, the potential of a smooth interface is considered to change in the cosine form

$$U(y) = \frac{U_1 + U_2}{2} + \frac{U_1 - U_2}{2} \cos\left(\frac{y - y_0 + \Delta N/2}{\Delta N}\pi\right),$$

and the smoothness of the interface is expressed by the width of the interface area ΔN. The larger the ΔN, the smoother the potential energy interface.

In Fig. 4, the conductance of QVHK and QSVHK states, $G_{\rm QV}$ and $G_{\rm QSV}$, versus Anderson disorder strength $W_{\rm NAD}$ and $W_{\rm MAD}$ are presented for smooth interfaces. As the width ΔN increases, the conductance $G_{\rm QV}$ gradually approaches the quantized value under non-magnetic Anderson disorder, as shown in Fig. 4(a). Non-zero ΔN separates the QVHK states in space, effectively suppressing the backscattering at the interface, as shown in the illustration in Fig. 4(a). The density of states ρ is determined by the square of the wavefunction ($|\phi|^2$) of the kink state in a clean ribbon. However, $G_{\rm QSV}$ is immune to the influence of ΔN since the states are well separated in space. The emergence of a narrow region where $\lambda_{\rm SOC} > |U(y)|$ transforms the QVH–QVH system into a QVH–QSH–QVH system. Imaging this transformation in Fig. 1(c), the domain wall is replaced by a narrow QSH region in Fig. 1(b), leading to the evolution of QVHK states into QSVHK states in Fig. 1(d). When ΔN is large enough, $G_{\rm QV}$ exhibits quantized values, similar to $G_{\rm QSV}$. Furthermore, under magnetic Anderson disorder, the introduction of a non-zero ΔN can also improve the transmission of QVHK and QSVHK states. As ΔN progressively increases, the influence of magnetic Anderson disorder on the quantized conductance diminishes. Notably, at $\Delta N = 20$, both $G_{\rm QV}$ and $G_{\rm QSV}$ can maintain their quantized values, even in the presence of a magnetic Anderson disorder with $W_{\rm MAD} = 0.2$ eV.

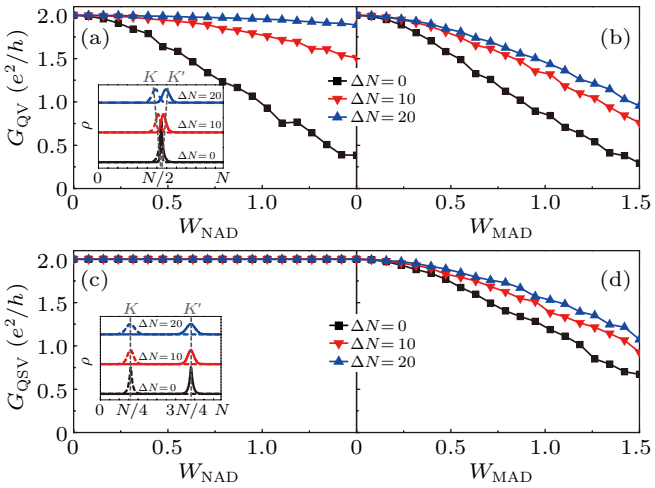


Fig. 4. The conductances G_{QV} and G_{QSV} vary with Anderson disorder strength W_{NAD} and W_{MAD} at different widths ΔN. Under different ΔN, the valley-resolved density of QVHK and QSVHK states ρ are interpolated in panels (a) and (c). The Fermi energy is $E = 0$. Other parameters are the same as in Fig. 2.

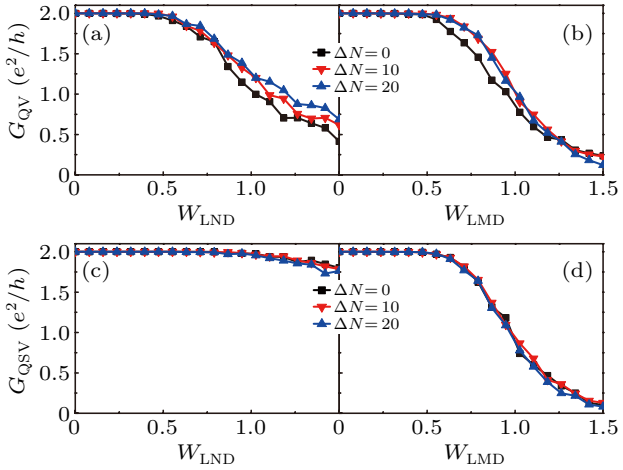


Fig. 5. The conductance G_{QV} and G_{QSV} versus long-range disorder strength W_{LND} and W_{LMD} at different widths ΔN. Other parameters are the same as in Fig. 2.

In contrast to the notable impact of increased ΔN on G_{QV} and G_{QSV} under Anderson disorder, ΔN exhibits minimal influence on G_{QV} and G_{QSV} under long-range disorder, as illustrated in Fig. 5. In precise terms, the conductance G_{QV} of the QVHK states exhibits a slow increase with the ascent of ΔN, whereas ΔN almost has no effect on the conductance G_{QSV} of QSVHK states. Comparing the conductances across all types of disorder in Figs. 4 and 5, it becomes apparent that the nonzero ΔN prompts G_{QV} to manifest behavior akin to G_{QSV}. This evolution is particularly pronounced in the case of Anderson disorder, as illustrated in Figs. 4(a) and 4(b).

3.3. Spin–valley filter

From the above discussion, we learned that the conductance of QSH edge states is destroyed easily by magnetic disorder due to broken time-reversal symmetry. In contrast, the conductance of QSVHK states protected by both space-inversion and time-reversal symmetries, remains quantized against either non-magnetic Anderson disorder, long-range non-magnetic disorder, or long-range magnetic disorder, as depicted in Figs. 2(a)–2(d). Lighted by the transport characteristic of QSH edge states and QSVHK states, we propose a spin–valley filter, where a single QSVHK state with specific valley and spin indices can be obtained at the interface of the QSH–QVH heterostructure. Also note that, in the former mentioned device hosting QSVHK states in Fig. 1(d), there is a pair of states following rightward with both valley K (spin-down) and valley K' (spin-up), respectively.

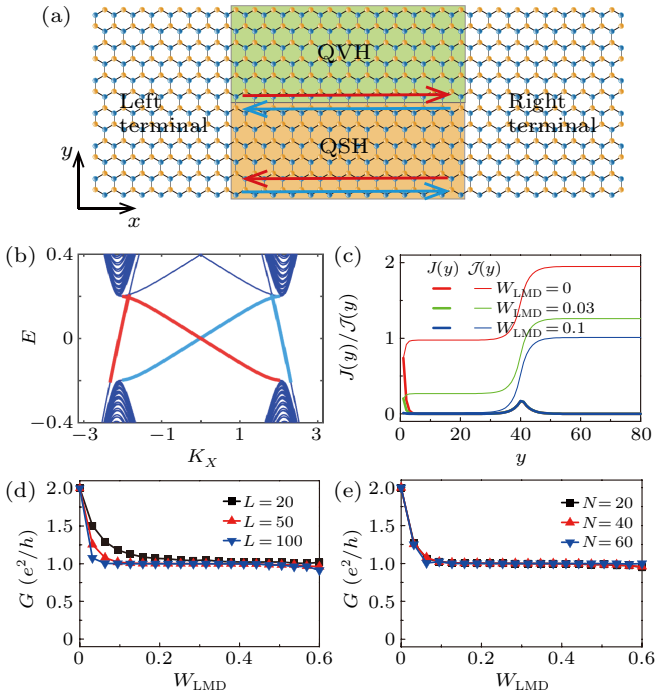


Fig. 6. (a) The schematic of the spin–valley filter. The red and the blue arrows represent the spin-up and the spin-down states, respectively. (b) The energy band of the central region. (c) Local current distributions $J(y)$ and the summation of local current distributions $\mathcal{J}(y) = \sum_{y_0=1}^{y} J(y_0)$ along the y direction from bottom to top under different long-range disorder strength W_{LMD}, respectively. The sample size is $L = 50$, $N(\text{QSH}) = N(\text{QVH}) = N = 40$. (d) The differential conductance G as a function of W_{LMD} for different length L of the central region. The width of the central region is $N = 40$. (e) The differential conductance G as a function of W_{LMD} for different width N, while the length is $L = 50$. The staggered potential is $U = (U_2 - U_1)\Theta(y - y_0) + U_1$ with $U_1 = 0.4$ eV and $U_2 = 0$ eV. The spin–orbit coupling strength is $\lambda_{SOC} = 0.2$ eV and the Fermi energy is $E = 0$.

The filter model is constructed by a line junction sandwiched by left and right terminals as displayed in Fig. 6(a). The central region functions as the spin–valley filter. Since the limited effect of smooth interface for QSVHK states under magnetic disorder, in the following calculation, a step-change interface is adopted. In the absence of disorder, the QSVHK state appears at the interface of the QSH and QVH regions, while the QSH edge state emerges at the opposite boundary of the QSH region, as illustrated in Figs. 6(a) and 6(b). The spin-up and spin-down states are denoted by red and blue arrows, respectively. Specifically, for QSVHK states in the middle of the ribbon, the spin-up carriers at valley K flow in the forward direction, while the spin-down carriers at K' valley move in

the opposite direction. In QSH edge states at the boom of the ribbon, the carriers with the spin-down flow in the forward direction, while the carriers with the spin-up flow in the opposite direction. By introducing the long-range magnetic disorder, it is expected that the QSH edge states damp rapidly, while the QSVHK states exhibit robustness. The valley index of the QSVHK state can be switched by the staggered potential which can be altered via an external electric field and the spin index is determined by the intrinsic spin–orbit coupling strength $\lambda_{\rm SOC}$. Consequently, a spin–valley filter with a controllable output is realized and the current flow is localized in the middle of the device.

To support the above discussed speculation, the current distribution is displayed in Fig. 6(c). Here, both spacial current distribution $J(y)$ (along the vertical direction) and its accumulation $\mathcal{J}(y)=\sum_{y_0=1}^{y}J(y_0)$ are displayed for different disorder strength. For a clean sample, i.e., $W_{\rm LMD}=0$, the current $J(y)$ peaks both in the middle of the ribbon and at the edge of the ribbon, the two peaks are for the QSVHK state and the QSH state, respectively. Also, the current carried by the QSVHK state is comparatively expanded in space. Across the whole ribbon, the current summation $\mathcal{J}(y)$ approaches $(e\Delta V)2e/h$, indicating a conductance of $2e^2/h$ contributed by QSVHK state and the QSH state. When the disorder is present (e.g., $W_{\rm LMD}=0.03$ and $W_{\rm LMD}=0.1$), the current carried by the QSVHK state stays unchanged and the current carried by the QSH state is damaged. Especially when $W_{\rm LMD}=0.1$, the transport contribution of QSH state is totally destroyed, the corresponding current peak disappears and its accumulation $\mathcal{J}(y)$ equals to $(e\Delta V)e/h$, signifying a single channel from the QSVHK state.

Next, we study how the efficiency of the filter is affected by the sample size. In Fig. 6(d), the curves for G versus $W_{\rm LMD}$ are shown for different sample lengths L. As the disorder strength $W_{\rm LMD}$ is enhanced, the conductance G attenuates from $2e^2/h$ and G saturates to e^2/h for larger $W_{\rm LMD}$. When the central region becomes longer, the attenuation process becomes faster. For example, when $L=50$ (~ 27.6 nm) and $N=40$ (~ 38.3 nm) there is only a single QSVHK channel available for $W_{\rm LMD}=0.1$, in agreement with the results in Fig. 6(c). When $L=100$ (~ 55.3 nm), to achieve the same goal, the disorder strength could be as small as $W_{\rm LMD}=0.05$. In Fig. 6(e), G versus $W_{\rm LMD}$ relations are shown for different sample widths N. It is easy to notice that the conductance of the device is immune to the width N. A device with width $N=20$ (~ 19.1 nm) is capable of functioning as a spin–valley filter. The result is quite reasonable since the QSVHK states and QSH states are well separated in space (see Fig. 6(c)) and the scattering between them is rather weak. In short, the device can work well under weak disorder and the size can be as small as 19.1 nm × 27.6 nm.

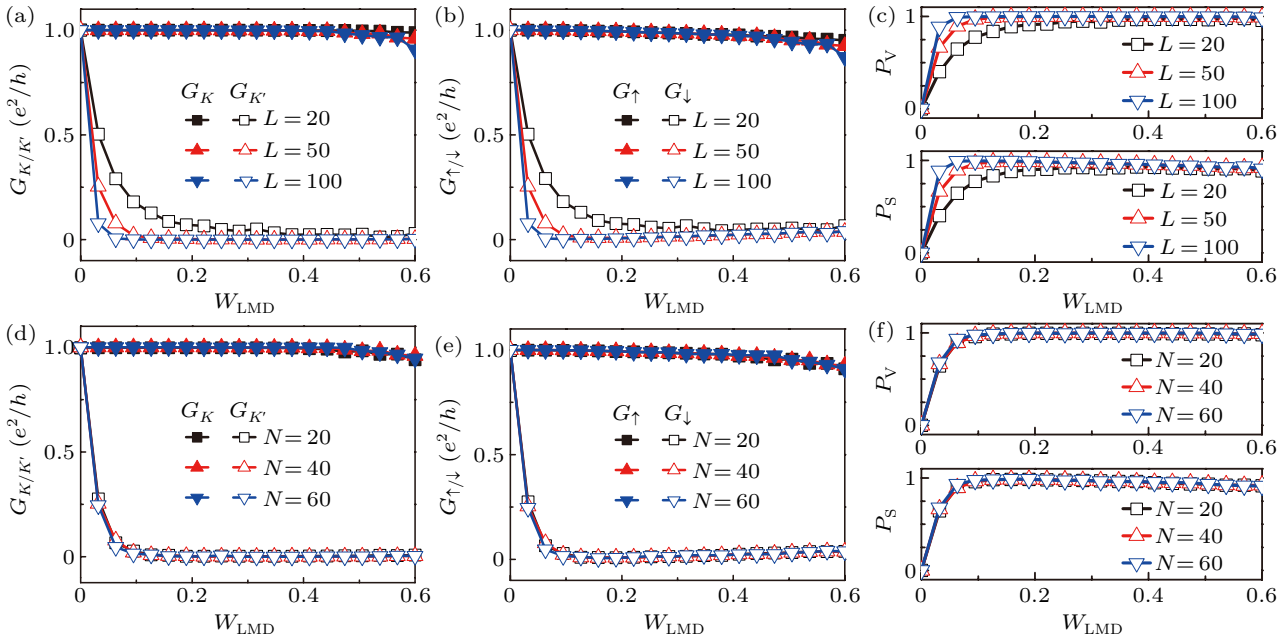


Fig. 7. Valley-resolved conductance ($G_{K/K'}$), spin-resolved conductance ($G_{\uparrow/\downarrow}$), valley polarization $P_{\rm V}$ and spin polarization $P_{\rm S}$ for different length L and width N. In panels (a)–(c), the width is $N=40$. In panels (d)–(f), the length of the central region is $L=50$. Other parameters are the same as in Fig. 6.

To provide more compelling evidence, the valley-resolved conductance and spin-resolved conductance of the same device are studied in Fig. 7. Here, both spin-resolved conductance ($G_\uparrow+G_\downarrow=G$) and valley-resolved conductance ($G_K+G_{K'}=G$), calculated by the method outlined in Section 2, validate the transport properties of the spin–valley filter. Here, the polarization $P_{\rm S}$ [$P_{\rm S}=(G_\uparrow-G_\downarrow)/G$] and $P_{\rm V}$ [$P_{\rm V}=(G_K-G_{K'})/G$] are defined to demonstrate the efficient

of the spin–valley filter.[29,58–60] In Fig. 7(a), as W_{LMD} in the filter increases, the quantized value of G_K remains unchanged, while $G_{K'}$ rapidly decreases from e^2/h to 0. Meanwhile, in Fig. 7(c) the upper panel, the valley polarization P_{V} increases from 0 to 1 as W_{LMD} is enhanced. The process is more rapid for longer samples (e.g., $L = 100$). A similar situation happens for the spin-resolved conductance in Figs. 7(b) and 7(c). The result indicates that the current is completely spin–valley polarized and only the carriers with spin-up at K valley can flow from the left terminal to the right terminal. When W_{LMD} increases further, P_{V} remains at $1e^2/h$, and the P_{S} only decreases slightly.

Although in the QVH–QSH–QVH structure (see Fig. 1(d)), we can also obtain spatially separated spin–valley states, it requires that the two interfaces are far enough apart so that the QSVHK states at the two interfaces do not interfere with each other. What's more, from an application perspective, in such a case only a wider sample can facilitate the terminal connection through which a branch of two QSVHK states has been drawn off. However, in our proposed spin–valley filter, the width of the nanoribbons does not need to be that large, and the nanoribbon width can be as narrow as 19.1 nm. Taking into account the inevitable electronic disorder, the present proposed device has even more advantages.

4. Conclusion

We select bismuthene as an ideal candidate for the spin–valley filter. The primary reason is that bismuthene is a graphene-like material with a large bulk gap and has been realized in experiments.[30] The second reason is that it has wide-range adjustable parameters, thus can be manipulated to produce a variety of Hall-type quantum states, and their combination can have new transport properties at the interfaces. By adjusting the parameters, we theoretically demonstrate the emergence of QSH edge, QVHK, and QSVHK states. The transport properties of QSH edge states and QVHK states are susceptible to magnetic disorder and Anderson disorder, respectively. In contrast, the conductance of QSVHK states remains quantized under both magnetic disorder and Anderson disorder. Based on the transport characteristics of QSH edge and QSVHK states achieved above, a spin–valley filter which generates a fully spin- and valley-polarized current is proposed. The valley index and spin index of the filter are determined by the staggered potential and the intrinsic spin–orbit coupling, respectively. Benefiting from the sensitivity of QSH state to magnetic disorder, the spin–valley filter is able to work under weak disorder and meanwhile, with a rather small device size. The valley- and spin-resolved conductances are calculated on these states and the results explicitly indicate that for a specific branch of spin and valley indexes, the related component in the current is robust and other components quickly damp to zero. When the disorder becomes much stronger, the valley polarization of the current remains at the unit, and the spin polarization is only weakly diminished.

Acknowledgments

We thank L. Xv and M. X. Zhai for their helpful discussions. Project supported by the National Natural Science Foundation of China (Grant No. 12104012), the Natural Science Foundation of Anhui Province of China (Grant No. 2108085MB42), the Key Research and Development Plan of Anhui Province of China (Grant No. 202104a05020048), the Major Science and Technology Project of Anhui Province of China (Grant No. 2021e03020007), and the Doctor Foundation of Anhui Jianzhu University (Grant No. 2019QDZ45).

References

[1] Haldane F D M 1988 *Phys. Rev. Lett.* **61** 2015
[2] Kane C L and Mele E J 2005 *Phys. Rev. Lett.* **95** 226801
[3] Gorbachev R V, Song J C W, Yu G L, Kretinin A V, Withers F, Cao Y, Mishchenko A, Grigorieva I V, Novoselov K S, Levitov L S and Geim A K 2014 *Science* **346** 448
[4] Sui M, Chen G, Ma L, Shan W Y, Tian D, Watanabe K, Taniguchi T, Jin X, Yao W, Di X D and Zhang Y 2015 *Nat. Phys.* **11** 1027
[5] Shimazaki Y, Yamamoto M, Borzenets I V, Watanabe K, Taniguchi T and Tarucha S 1988 *Nat. Phys.* **11** 1032
[6] Geisenhof F R, Winterer F, Seiler A M, Lenz J, Martin I and Weitz R T 2022 *Nat. Commun.* **95** 226801
[7] Cheng S G, Liu H, Jiang H, Sun Q F and Xie X C 2018 *Phys. Rev. Lett.* **121** 156801
[8] Hasan M Z and Kane C L 2010 *Rev. Mod. Phys.* **82** 3015
[9] Yan B and Zhang S C 2012 *Rep. Prog. Phys.* **75** 096501
[10] Murakami S, Nagaosa N and Zhang S C 2004 *Phys. Rev. Lett.* **93** 156804
[11] Bernevig B A, Hughes T L and Zhang S C 2006 *Science* **314** 5806
[12] Kane C L and Mele E J 2005 *Phys. Rev. Lett.* **95** 146802
[13] Yao W, Xiao D and Niu Q 2008 *Phys. Rev. B* **77** 235406
[14] Cao T, Wang G, Han W, Ye H, Zhu C, Shi J, Niu Q, Tan P, Wang E, Liu B and Feng J 2012 *Nat. Commun.* **3** 887
[15] Cheng S G, Zhou J, Jiang H and Sun Q F 2016 *New J. Phys.* **18** 103024
[16] Yin L J, Jiang H, Qiao J B and He L 2016 *Nat. Commun.* **7** 11760
[17] Ezawa M 2015 *J. Phys. Soc. Jpn.* **84** 121003
[18] Jatiyanon K and Soodchomshom B 2018 *Superlattices Microstruct.* **120** 540
[19] Ezawa M 2013 *Phys. Rev. B* **88** 161406
[20] Neto A H C, Guinea F, Peres N M R, Novoselov K S and Geim A K 2009 *Rev. Mod. Phys.* **81** 109
[21] Aufray B, Kara A, Vizzini S, Oughaddou H, Léandri C, Ealet B and Lay G L 2010 *Appl. Phys. Lett.* **96** 183102
[22] Mak K F, Lee C, Hone J, Shan J and Heinz T F 2010 *Phys. Rev. Lett.* **105** 136805
[23] Sichau J, Prada M, Anlauf T, Lyon T J, Bosnjak B, Tiemann L and Blick R H 2019 *Phys. Rev. Lett.* **122** 046403
[24] Zhang S, Guo S, Chen Z, Wang Y, Gao H, Gómez-Herrero J, Ares P, Zamora F, Zhu Z and Zeng H 2018 *Chem. Soc. Rev.* **47** 9821021
[25] Gui R, Jin H, Sun J, Jiang X and Sun Z 2019 *J. Mater. Chem. A* **7** 25712
[26] Ji J, Song X, Liu J, Yan Z, Huo C, Zhang S, Su M, Liao L, Wang W, Ni Z, Hao Y and Zeng H 2016 *Nat. Commun.* **7** 13352
[27] Xu G, Zhou T, Scharf B and Žutić I 2020 *Phys. Rev. Lett.* **125** 157402
[28] Zhang S H, Yang W and Chang K 2018 *Phys. Rev. B* **97** 085420
[29] Cheng S G, Zhang R Z, Zhou J, Jiang H and Sun Q F 2018 *Phys. Rev. B* **97** 085420
[30] Reis F, Li G, Dudy L, Bauernfeind M, Glass S, Hanke W, Thomale R, Schäfer J and Claessen R 2017 *Science* **357** 287
[31] Isaeva A, Rasche B and Ruck M 2013 *Phys. Status Solidi Rapid Res. Lett.* **7** 39

[32] Rasche B, Isaeva A, Ruck M, Borisenko S, Zabolotnyy V, Büchner B, Koepernik K, Ortix C, Richter M and van den Brink J 2013 *Nat. Mater.* **12** 422

[33] Song Z, Liu C C, Yang J, Han J, Ye M, Fu B, Yang Y, Niu Q, Lu J and Yao Y 2014 *NPG Asia Mater.* **6** e147

[34] Zhou T, Zhang J, Jiang H, Žutić I and Yang Z 2018 *NPJ Quantum Mater.* **3** 39

[35] Zhou J, Zhou T, Cheng S G, Jiang H and Yang Z 2019 *Phys. Rev. B* **99** 195422

[36] Xiao D, Yao W and Niu Q 2007 *Phys. Rev. Lett.* **99** 236809

[37] Zeng H, Dai J, Yao W, Xiao D and Cui X 2012 *Nat. Nanotechnol.* **7** 490

[38] Wang Y, Deng L, Wei Q, Wan Y, Liu Z, Lu X, Li Y, Bi L, Zhang L, Lu H, Chen H, Zhou P, Zhang L, Cheng Y, Zhao X, Ye Y, Huang W, Pennycook S J, Loh K P and Peng B 2020 *Nano Lett.* **20** 2129

[39] Liu Z, Feng W, Xin H, Gao Y, Liu P, Yao Y, Wenggh H and Zhao J 2019 *Mater. Horiz.* **6** 781

[40] Li J, Wang K, McFaul K J, Zern Z, Ren Y, Watanabe K, Taniguchi T, Qiao Z and Zhu J 2016 *Nat. Nanotechnol.* **11** 1060

[41] Pan H, Li X, Zhang F and Yang S A 2015 *Phys. Rev. B* **92** 041404

[42] Zhou T, Zhang J, Xue Y, Zhao B, Zhang H, Jiang H and Yang Z 2016 *Phys. Rev. B* **94** 235449

[43] Mannix A J, Kiraly B, Hersam M C and Guisinger N P 2017 *Nat. Rev. Chem.* **1** 0014

[44] Datta S 1995 *Electronic transport in mesoscopic systems* (Cambridge: Cambridge University Press) pp. 117–174

[45] Ando T 1989 *Phys. Rev. B* **40** 5325

[46] Lee D H and Joannopoulos J D 1981 *Phys. Rev. B* **23** 4997

[47] Sancho M P L, Sancho J M L and Rubio J 1984 *J. Phys. F* **14** 1205

[48] Sancho M P L, Sancho J M L and Rubio J 1985 *J. Phys. F* **15** 851

[49] Jiang H, Wang L, Sun Q F and Xie X C 2009 *Phys. Rev. B* **80** 165316

[50] Zhang Y, Hu J P, Bernevig B A, Wang X R, Xie X C and Liu W M 2008 *Phys. Rev. B* **78** 155413

[51] Zhang J, Zhang Z Q, Cheng S G and Jiang H 2022 *Phys. Rev. B* **106** 195304

[52] Ando T 1991 *Phys. Rev. B* **44** 8017

[53] Zhang S H, Yang W and Chang K 2017 *Phys. Rev. B* **95** 075421

[54] Zhou T, Cheng S, Schleenvoigt M, Schüffelgen P, Jiang H, Yang Z and Žutić I 2021 *Phys. Rev. Lett.* **127** 116402

[55] König M, Wiedmann S, Brüune C, Roth A, Buhmann H, Molenkamp L W, Qi X L and Zhang S C 2007 *Science* **318** 766

[56] Culcer D, Keser A C, Li Y and Tkachov G 2020 *2D Mater.* **7** 022007

[57] Ju L, Shi Z, Nair N, Lv Y, Jin C, Jr J V, Ojeda-Aristizabal C, Bechtel H A, Martin M C, Zettl A, Analytis J and Wang F 2015 *Nature* **520** 650

[58] Rycerz A, Tworzydło J and Beenakker C 2007 *Nat. Phys.* **3** 172

[59] Liu Y, Song J, Li Y, Liu Y and Sun Q F 2013 *Phys. Rev. B* **87** 195445

[60] da Costa D R, Chaves A, Sena S H R, Farias G A and Peeters F M 2015 *Phys. Rev. B* **92** 045417